NUMERICAL ANALYSIS OF MECHANICAL BEHAVIOR DURING FRICTION STIR WELDING

S. MAEDA*, K. IKUSHIMA*, M. SHIBAHARA*

**Graduate school of engineering, Osaka Metropolitan University, Japan*

DOI 10.3217/978-3-99161-089-2-015, license CC BY 4.0

ABSTRACT

A novel numerical analysis method based on a Coupled Eulerian–Lagrangian (CEL) approach with an implicit formulation was developed to simulate the transient thermal and mechanical behavior during Friction Stir Welding (FSW). The proposed method combines an operator-split-based CEL scheme with a dynamic implicit solver optimized for GPU-based parallel computation, enabling stable and accurate simulations with over 1.2 million nodes. This approach permits larger time steps than conventional explicit methods without sacrificing accuracy, achieving a computational cost of about 5.5 hours for each simulated second of welding. The simulation results successfully reproduced key features observed in experiments, including periodic temperature and load fluctuations associated with tool rotation, which are characteristic of onion ring formation. Furthermore, by varying the tool tilt angle, the influence of tool orientation on thermal fields, material flow, and defect generation was quantitatively investigated. A forward tool tilt was found to move the high-temperature region to the front of the tool, leading to the formation of tunnel defects. This provided insight into the defect formation mechanism by revealing that a forward tilt alters material flow and thermal concentration in a way that promotes tunnel defects. These findings demonstrate the effectiveness of the proposed method in capturing complex thermo-mechanical phenomena during FSW and its potential for optimizing welding parameters and improving joint quality.

Keywords: Friction Stir Welding, Coupled Eulerian-Lagrangian method, Thermal elastic-plastic analysis, Implicit formulation

INTRODUCTION

Friction Stir Welding (FSW) has become a widely adopted joining technique for lightweight metal materials due to its superior mechanical strength and reduced thermal impact. In this process, a rotating and downward-pressured tool travels along the joint line, inducing plastic flow in the material and achieving solid-state bonding. However, the material behavior during FSW is strongly thermo-mechanically coupled, and it remains challenging to accurately capture the thermal, mechanical, and material flow behavior, particularly in the stirred region.

In addition, improper material flow or thermal history during welding can lead to the formation of defects such as tunnel defects and voids. These defects can significantly reduce the structural reliability of the weld, making it essential to predict and prevent such defects in FSW. In addition, concentric patterns, commonly referred to as “onion rings” [1], are sometimes observed on the surface or in cross-sections of the weld, and are considered characteristic features of the process. These structures are believed to indicate the periodic, layered flow of material and have been considered a physical record of the plastic deformation and stirring behavior during welding [2]. However, the detailed mechanism of their formation has not yet been fully clarified.

In recent years, the Coupled Eulerian-Lagrangian (CEL) method [3] has been widely used as an effective approach for analyzing the complex material flow and large deformations that occur during the Friction Stir Welding (FSW) process. The CEL method is capable of accurately handling large material deformations, multi-body contact, and interfacial friction and plastic deformation, making it particularly attractive for reproducing the detailed thermal and mechanical behavior during FSW [4,5]. In particular, ABAQUS/Explicit has been widely used as a finite element analysis software that supports CEL implementation [6], and many previous studies have adopted it [7-13]. Furthermore, in addressing the challenge of high computational cost, some attempts have been made to balance accuracy and efficiency by appropriately applying mass scaling techniques [7,8].

On the other hand, the periodic phenomena specific to FSW require more detailed analysis [8]. To achieve this, it is essential to develop computational environments capable of high-accuracy simulations and to further accelerate the computation. In fact, it has been reported that current simulations involving 200,000 to 300,000 elements require approximately two days to analyze just one second of the process [9,10], indicating that the high computational cost remains a significant challenge for practical applications. If further improvements in simulation accuracy and speed can be achieved, it will become possible to investigate conditions closer to actual processing environments. This is expected to be useful for selecting and optimizing welding parameters, including stirring behavior and periodic phenomena.

In this study, a novel CEL analysis method based on an implicit formulation was developed to accurately and stably capture the transient thermal and mechanical responses during FSW. Compared to conventional explicit methods, the proposed method allows for larger time steps while maintaining computational accuracy, thereby enabling numerically stable simulations. Furthermore, by incorporating GPU-based parallel computation, the method achieves high-speed analysis within practical computation time, even when using a fine mesh resolution. To validate the effectiveness of the proposed method, it was applied to Friction Stir Processing (FSP) of a single plate, and the spatial distributions and time histories of the temperature field, mechanical responses, and stirring behavior were visualized and examined. In addition, the periodic nature inherent in these phenomena was also investigated through the analysis. Additionally, a qualitative comparison with previous experimental results was conducted to evaluate the accuracy and practical applicability of the simulation outcomes. Moreover, simulations with varying tool tilt angles were performed to investigate the influence of tool angle on the temperature field and defect formation, and to explore the mechanisms behind defect generation.

IMPLICITLY FORMULATED CEL-BASED NUMERICAL ANALYSIS METHOD FOR THE FRICTION STIR WELDING PROCESS

All numerical simulations were performed using an in-house finite element code developed by the authors, in which the Coupled Eulerian-Lagrangian (CEL) framework and the implicit dynamic scheme were implemented based on established numerical methods. In this study, a finite element method (FEM)-based analysis approach grounded in solid mechanics was developed to investigate the mechanical behavior during FSW. The analysis employed the CEL method, which integrates both Lagrangian and Eulerian formulations. Fig. 1 presents the overall analysis flow. As shown in Fig. 1, thermal conduction analysis and thermal elastic-plastic analysis were sequentially performed while accounting for mutual contact between the Eulerian and Lagrangian domains, where meshes are assigned to space and material, respectively. The two analyses were coupled via advection calculations, enabling stable simulation of large deformations occurring near the weld zone during FSW. In the Lagrangian analysis, since the mesh is assigned to the object, it is possible to investigate the effects of geometric changes. However, this approach can suffer from mesh distortion or failure under large deformations, making it unsuitable for severe material flow. In contrast, the Eulerian formulation assigns the mesh to space, and physical variables remain fixed within the spatial domain, allowing stable analysis even when material flow crosses mesh boundaries. In this study, the joining tool, which undergoes relatively small deformation, was modeled using the Lagrangian formulation, while the heavily stirred workpiece material was modeled using the Eulerian formulation.

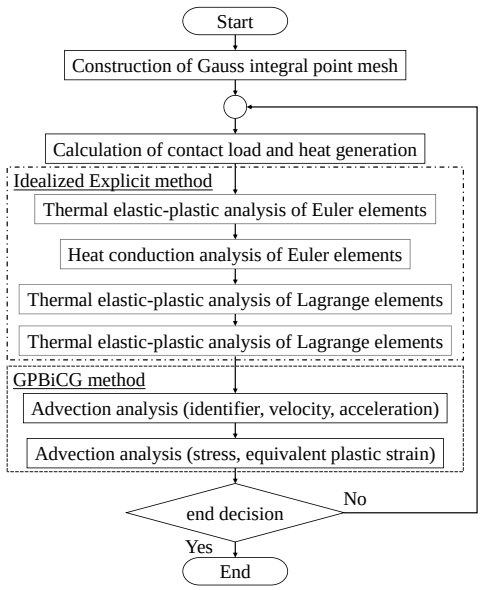

Fig. 1 Analysis flow of development

COUPLED EULERIAN–LAGRANGIAN METHOD USING THE OPERATOR SPLIT APPROACH

In this study, a FEM-based analysis approach was developed based on solid mechanics. The friction stir welding (FSW) phenomenon of material deformation is assumed to be governed by the following fundamental equations of solid mechanics.

$$\rho \frac{\partial v_i(X,t)}{\partial t} + \frac{\partial \sigma_{ij}}{\partial x_j} = f_i \tag{1}$$

Here, ρ denotes the density, $\boldsymbol{v}$ the velocity vector, $\boldsymbol{\sigma}$ the stress tensor, $\boldsymbol{x}$ the spatial coordinate, and $\boldsymbol{f}$ the body force. The subscripts i and j indicate the directional components of each variable. During FSW, large localized strains occur; thus, by applying the material derivative to Equation (1), both temporal and spatial variations of the velocity field can be simultaneously considered, leading to the following form:

$$\rho\left(\frac{\partial v_i(x,t)}{\partial t} + v_j \frac{\partial v_i}{\partial x_j}\right) + \frac{\partial \sigma_{ij}}{\partial x_j} = f_i \tag{2}$$

At this stage, the left-hand side of the equation can be divided into a temporal derivative term, an advection term, and a stress gradient term. In this study, the operator-splitting method [14] was applied to Equation (2), whereby Equation (3), expressed in the Lagrangian formulation - where each computational point moves directly - is solved together with Equation (4), expressed in the Eulerian formulation, which computes physical quantities at fixed spatial locations.

$$\rho \frac{\partial v_i(x,t)}{\partial t} + \frac{\partial \sigma_{ij}}{\partial x_j} = f_i \tag{3}$$

$$\frac{\partial v_i(x,t)}{\partial t} + v_j \frac{\partial v_i}{\partial x_j} = 0 \tag{4}$$

For the thermal elastic-plastic calculation in Equation (3), the Newmark-β method [15] was used for discretization, and Idealized Explicit FEM [16-18], which can account for dynamic effects, was adopted as the solver. For the advection calculation in Equation (4), a stabilized FEM based on the SUPG (Streamline Upwind Petrov-Galerkin) method [19,20] was employed, and the Wilson-θ method [21,22] was used for time discretization. The system of equations was solved using the GPBiCG (Generalized Product-type Bi-Conjugate Gradient) method [23,24]. Furthermore, GPU-based parallel computation was applied to both Idealized Explicit FEM and the GPBiCG solver to accelerate the computation [25,26].

Thus, a CEL-based numerical analysis method using a dynamic implicit scheme was developed to simulate the thermal and mechanical behavior during FSW.

INTERFACE REPRESENTATION USING THE VOLUME OF FLUID (VOF) METHOD

The interface of the workpiece material stirred by the tool was represented using the Volume of Fluid (VOF) method [27], which is commonly employed in Eulerian formulations for free-surface fluid flow. Using a solid interface identifier φ, the values were defined as follows: φ = 0.5 for the solid interface, φ = 0.0 for voids, and φ = 1.0 for solid material. The evolution of φ was calculated using Equation (5).

$$\frac{\partial \varphi}{\partial t} + v_j \frac{\partial \varphi}{\partial x_j} = 0 \quad (0.0 \le \varphi \le 1.0) \tag{5}$$

In addition, defects were evaluated by identifying regions where $\varphi < 0.5$ as defects, while regions with $\varphi \ge 0.5$ were displayed as the base material.

CONTACT MODEL

The contact and friction between the tool and the workpiece were determined based on the amount of penetration of the Lagrangian tool element into the Eulerian workpiece element, as illustrated in Fig. 2. The volumetric contact force f_c was calculated using the penalty method [28].

$$f_c = \alpha(T)\varphi\psi \tag{6}$$

Here, f_c denotes the magnitude of the contact force. $\alpha(T)$ is the penalty coefficient, and ψ is the solid interface identifier for the joining tool. The value of ψ was assigned as 0.0 at the outermost surface nodes of the tool, 1.0 at the next inner layer, and 2.0 at nodes further inside. Intermediate values between these layers were interpolated using shape functions. The penalty coefficient $\alpha(T)$ was varied based on the temperature-dependent Young's modulus $E(T)$. Using the volumetric contact force f_c calculated from Eq. (6), the body force F_{ci} for each element was computed using the following equation.

$$F_{c_i} = \int_{\Omega_e} f_{c'} n_i \, d\Omega \tag{7}$$

Here, Ω_e is the element volume, Ω is the total volume, and n_i is the normal vector.

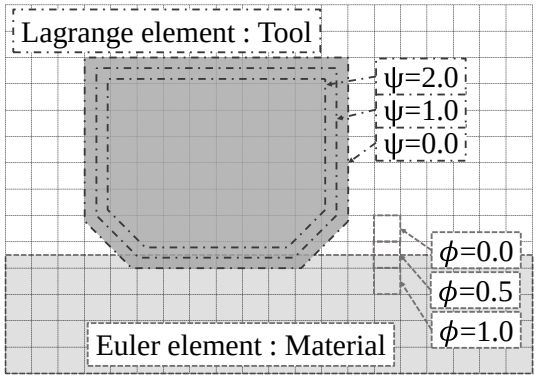

Fig. 2 Schematic of contact analysis

PLASTIC AND FRICTIONAL HEAT GENERATION MODELS

In this study, the heat generated during FSW is assumed to originate from two sources: plastic heat generation due to plastic deformation of the material, and frictional heat generation due to contact between the tool and the workpiece. Each is calculated as follows. The amount of plastic heat generation per element, q_p, is computed from the work done by plastic deformation in each element using the following equation.

$$q_p = \int \eta_p \bar{\sigma} \Delta \bar{\varepsilon}_p \, dV \tag{8}$$

Here, η_p, $\bar{\sigma}$, $\Delta\bar{\varepsilon}_p$, and V denote the conversion efficiency of plastic work into heat, equivalent stress, increment of equivalent plastic strain, and unit volume, respectively. In this study, η_p was assumed to be 90% [29,30], and the work generated by plastic deformation was converted into heat accordingly.

Additionally, the amount of frictional heat generation q_f at the contact interface was calculated using the frictional force F_f.

$$q_f = \int_s \eta_f \boldsymbol{F}_f \boldsymbol{v}_r \, dS \tag{9}$$

$$\boldsymbol{F}_f = \begin{cases} -\mu \left\| \boldsymbol{F}_c \right\| \dfrac{\boldsymbol{v}_r}{\left\| \boldsymbol{v}_r \right\|} & (0 \le \mu \left\| \boldsymbol{F}_c \right\| < f_{r_{\max}}(T)) \\ -f_{r_{\max}}(T) \dfrac{\boldsymbol{v}_r}{\left\| \boldsymbol{v}_r \right\|} & (f_{r_{\max}}(T) \le \mu \left\| \boldsymbol{F}_c \right\|) \end{cases} \tag{10}$$

Here, η_f is the thermal efficiency of frictional heat generation, $\boldsymbol{v}_r$ is the relative velocity between the joining tool and the workpiece material. The friction coefficient μ used in the contact model was set to 0.5, and η_f was assumed to be 100% [8,9,11-13]. The friction force

is directly formulated as a vector quantity based on the contact force magnitude f_c and the relative velocity, and its magnitude is limited by a temperature-dependent upper bound $f_{r\,max}(T)$, which was determined from the temperature-dependent yield stress $\sigma_Y(T)$.

Heat transfer to the surrounding environment was considered by applying a constant heat transfer coefficient of 0.01 W/m²·°C on the exposed surfaces of the workpiece. The same constant heat transfer coefficient, without temperature dependence, was also applied at the contact interface to account for heat conduction between the tool and the workpiece.

ELASTIC-PLASTIC MODEL

Although the Johnson–Cook model [31] is frequently used as the material model for FSW processes [8-13], in this study, the von Mises model [32] was employed for both the joining tool and the workpiece materials to calculate the plastic strain and stress during and after the transient joining process. This choice was made because the primary objective of the present study is to investigate the overall thermo-mechanical response, material flow behavior, and defect formation, for which the von Mises model is sufficient under the present processing conditions.

FSP ANALYSIS OF ALUMINUM ALLOY

Using the analysis method described in the previous chapter, the FSP process for an aluminum alloy AA5083 was simulated. The simulation included tool plunging, dwelling for material stabilization, welding, and tool retraction. The thermal and mechanical states of both the tool and the workpiece material were investigated.

ANALYSIS MODEL AND CONDITIONS

The geometry and dimensions of the analysis model are shown in Fig. 3. As illustrated in Fig. 3(a), the probe diameter, probe length, and shoulder diameter of the joining tool modeled using Lagrangian elements were set to 5.0 mm, 4.125 mm, and 15.0 mm, respectively. As shown in Fig. 3(b), the base material was modeled using Eulerian elements. The total domain size was set to 200.0 mm in length, 200.0 mm in width, and 14.0 mm in height, while the initial solid region was defined as 200.0 mm in length, 200.0 mm in width, and 4.0 mm in thickness. The minimum mesh size in the stirring zone was set to a cube with a side length of 0.2 mm. The number of nodes and elements in the tool is 5,772 and 5,020, respectively, while the number of nodes and elements in the Eulerian elements used for the space and the plate is 1,219,581 and 1,169,280, respectively. In this study, the x-, y-, and z-directions correspond to the welding, transverse, and normal directions, respectively.

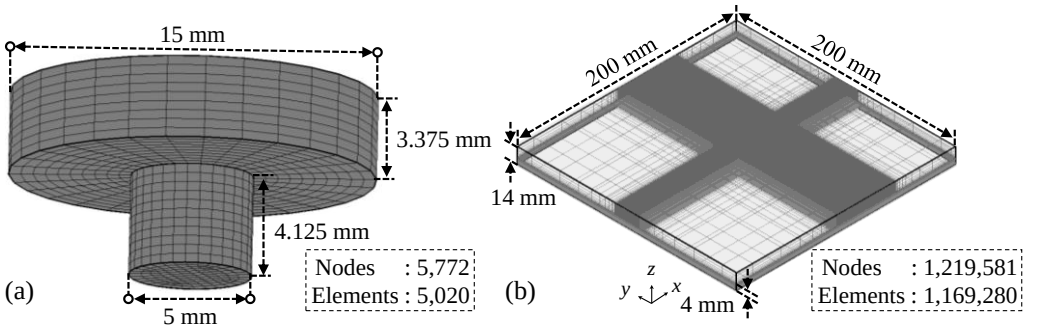

Fig. 3 Size and shape of FSW model. (a) Tool with Lagrangian elements. (b) Material with Eulerian elements

Aluminum alloy AA5083 was used as the workpiece material, and the tool was made of SDK61. The temperature-dependent material properties of AA5083 [33] and SDK61 [34-36] are shown in Figure 4, while the temperature-independent properties are summarized in Table 1. The material properties for SDK61 were determined by integrating data from multiple sources [34-36].

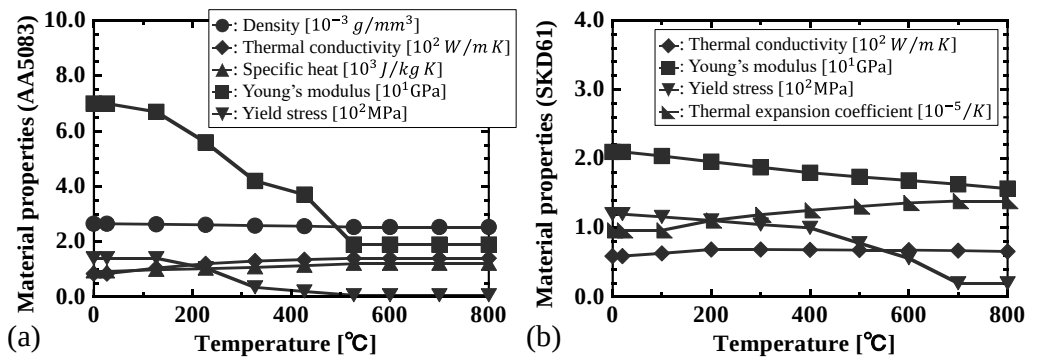

Fig. 4 Temperature-dependent material properties. (a) AA5083 for material [33]. (b) SDK61 for tool [34-36]

Table 1 Temperature-independent material properties used in the analysis. Properties marked as "Dependent" are treated as temperature-dependent and shown in Fig. 4.

Material	AA5083	SKD61
Density [g/mm^3]	Dependent (Fig. 4)	7.98×10^{-3}
Specific heat [J/kg K]	Dependent (Fig. 4)	461.0
Thermal expansion coefficient [1/K]	2.36×10^{-5}	Dependent (Fig. 4)
Poisson's ratio	0.33	0.28

Fig. 5 shows the entire process including plunging, dwelling, welding, and retraction. In the present analysis, the FSP process was simulated under displacement-controlled conditions, where the vertical position of the tool was prescribed throughout plunging, dwelling, and welding. As illustrated in the figure, the tool was inserted into the center of the workpiece, held in place for 10 seconds for stabilization, then advanced 40 mm for welding, and finally retracted. The tool's tilt angle was set to 3°, and its rotational speed was fixed at 500 rpm. The plunge depth at the tool center was set to 3.8 mm. The plunge speed, welding speed, and retraction speed were set to 15 mm/min, 250 mm/min, and 150 mm/min, respectively. The total duration of the process was approximately 38.52 seconds, with a time step of 0.002 seconds, resulting in a total of 19,260 computation steps. Displacement control was applied by imposing prescribed displacements on the nodes at the top surface of the tool to achieve tool rotation, translational movement, and holding. In addition, the displacement normal to the surfaces, including the sides and the bottom, was constrained.

Although the dwelling time of 10 seconds is longer than that typically used in practical FSW processes, it was selected to ensure that the thermal and mechanical fields reached a quasi-steady state prior to welding. This was confirmed in the present analysis by the saturation of the peak temperature beneath the tool and by the periodic, rotation-synchronized fluctuations in temperature and tool load without significant temporal drift. The present study focuses on the detailed investigation of transient and periodic thermo-mechanical behavior rather than optimization of computational efficiency; therefore, the time allocation among plunging, dwelling, and welding was not optimized for efficiency.

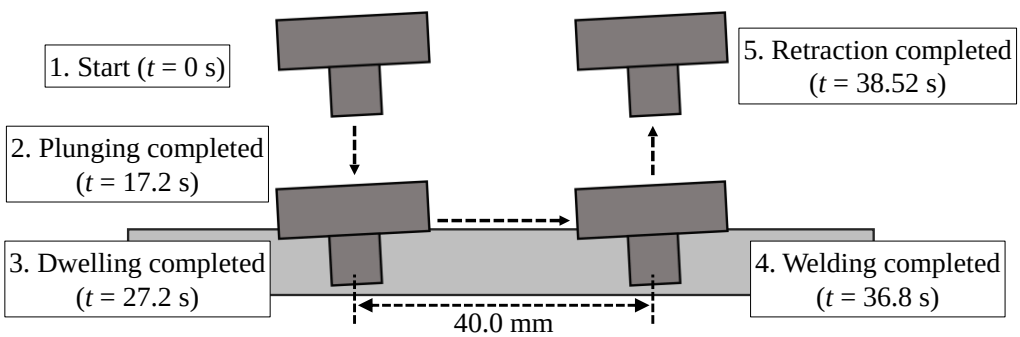

Fig. 5 Overview of all FSW processes for analysis

INVESTIGATION OF THERMAL AND FLOW BEHAVIOR OF THE WORKPIECE

Fig. 6 shows the heat generation density distribution on the surface of the base material during the tool plunging process. Figs. 6(a) through (d) correspond to changes in the distance between the center of the tool probe and the base material, illustrating the heat generation behavior at each stage. Fig. 6(a) shows the heat distribution at the moment when the center of the tool first contacts the base material. Due to the 3° tilt of the tool, significant heat generation is observed

on the rear side of the tool when the probe center contacts the surface. In Fig. 6(b), where the plunge depth reaches 1.0 mm, the heat distribution becomes axisymmetric as the tool plunges deeper, with an increase in heat generation particularly near the edge of the probe. In Fig. 6(c), at a plunge depth of 2.0 mm, the base material is pressed upward by the probe, resulting in contact with the shoulder. Additionally, the amount of heat generation near the probe edge decreases, which is likely due to a rise in temperature at the lower part of the probe as plunging progresses, thereby reducing frictional and plastic heat generation. In Fig. 6(d), where the plunge depth reaches 3.0 mm, heat generation on the rear side of the tool becomes dominant again due to the tool's tilt.

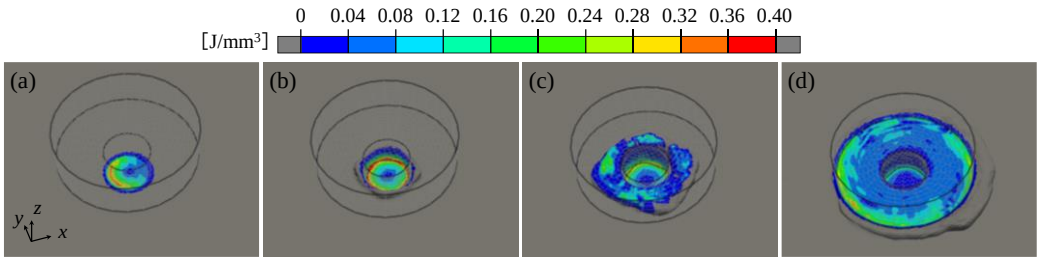

Fig. 6 Heat density distribution on plate surface according to insertion amount of pin center during tool plunging. (a) 0 mm. (b) 1.0 mm. (c) 2.0 mm. (d) 3.0 mm

Similarly, Fig. 7 shows the heat generation density distribution on the plate surface at the completion of tool plunging, after the dwelling phase, and during welding. From Fig. 7(a), it is evident that at the end of the tool plunging phase, greater heat generation occurs on the rear side of the tool due to its tilt, particularly at the surface where the shoulder contacts the plate. In addition, significant heat generation is observed at the contact point with the shoulder edge, where the peripheral speed is highest. In Fig. 7(b), after the dwelling phase, it can be seen that, similar to the plunging phase, heat generation at the shoulder contact area decreases due to the temperature increase. Furthermore, during the welding phase, as shown in Fig. 7(c), intense heat generation is observed on the front side of the tool - where it contacts the lower-temperature region of the plate - particularly at the outer edge of the shoulder, which has the highest peripheral speed.

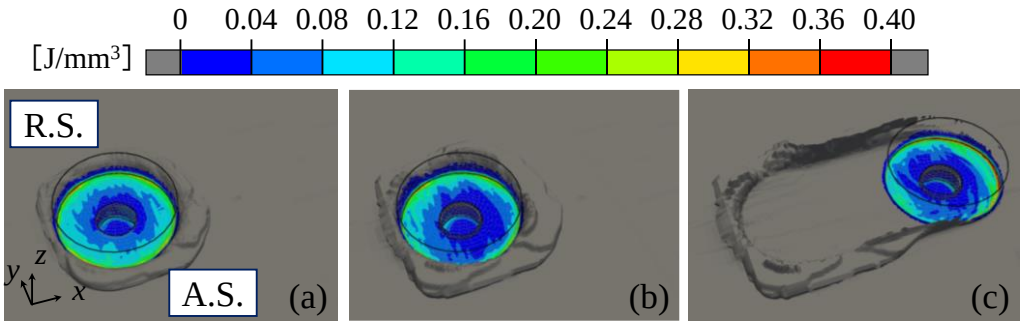

Fig. 7 Heat density distribution on plate surface at each stage after tool insertion completed. (a) Plunging completed. (b) Dwelling completed. (c) During welding

Fig. 8 shows the temperature distribution on the plate surface at the completion of tool plunging, after the dwelling phase, and during welding. The figure confirms that under the present analysis conditions, a high-temperature region exceeding 540 °C is formed directly beneath the tool throughout all process stages. Comparing Figs. 8(a) and (b), this indicates that the 10-second dwelling phase leads to an overall increase in the base material temperature. Furthermore, a comparison between Figs. 8(b) and (c) indicates that the temperature distribution formed during the dwelling phase is largely maintained as the welding progresses.

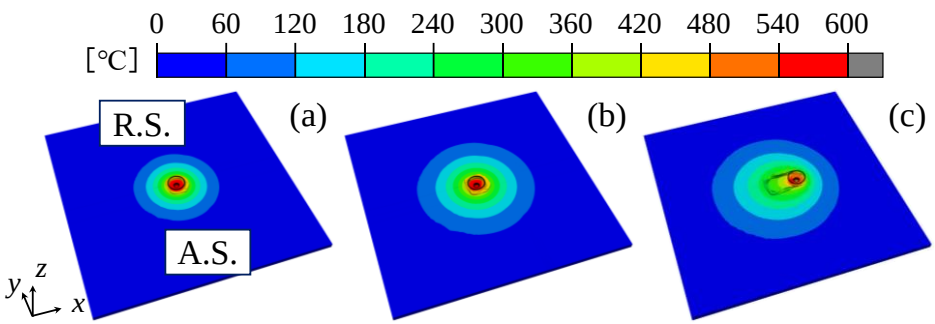

Fig. 8 Heat density distribution on plate surface at each stage after tool insertion completed. (a) Plunging completed. (b) Dwelling completed. (c) During welding

Fig. 9 shows the temperature distribution on the surface of the base material near the tool during one full rotation of the tool. Fig. 9(a) presents the state at 4.8 seconds after the start of welding, while Figs. 9(b)-(e) show the sequential changes during the subsequent 0.12 seconds, corresponding to one full rotation, divided into quarter-rotation intervals. These results show that due to the tilt of the tool, a high-temperature region is formed on the rear side beneath the tool. Furthermore, a comparison of Figs. 9(a)-(d) reveals that the region exceeding 520 °C moves along the rotation direction of the tool, following its motion. Comparing Figs. 9(a) and

(e), the temperature distributions appear nearly identical, indicating that under the current conditions, the temperature field varies periodically with each full rotation of the tool. This periodic behavior corresponds well with experimental observations that the spacing of onion rings matches the tool's advance per revolution [37]. The observed periodic temperature variation is considered to affect local plastic strain accumulation and material flow behavior, and thus may act as one of the contributing factors to onion-ring formation.

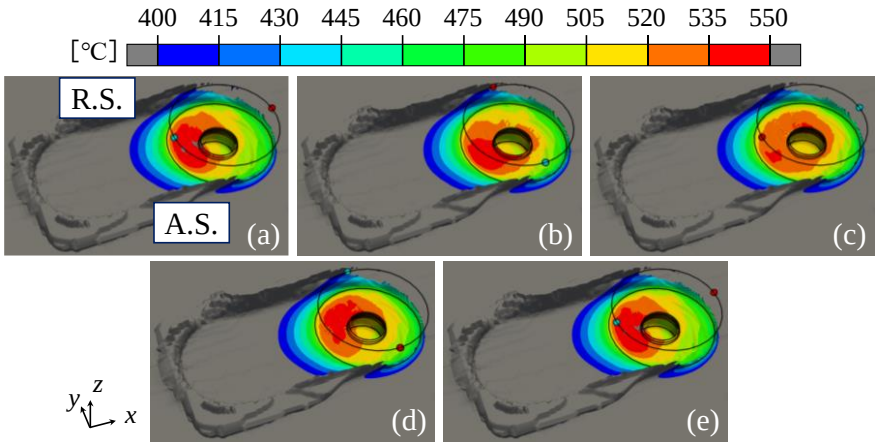

Fig. 9 Temperature distribution on the plate surface during one rotation of tool. (a) Start of rotation. (b) 1/4 rotation. (c) 1/2 rotation. (d) 3/4 rotation. (e) 1 rotation

Next, in order to examine the material flow during stirring, Fig. 10 shows the temperature distribution and flow velocity distribution on the cross-section at the tool center over a tool rotation (0.12 s) starting from 9.1 seconds after the beginning of welding. In the figure, the contour represents the temperature distribution, while the arrows indicate the direction of material flow within the cross-section at each node. The size of the arrows represent the magnitude of the three-dimensional velocity. As observed on the top surface in Fig. 9, the temperature distribution also changes in the thickness direction following the tool rotation. Similarly, the material flow exhibits periodic behavior synchronized with the tool rotation. In addition, it is evident that high material flow velocities occur near the tool and in regions of high temperature, with the flow velocity on the retreating side (R.S.) being greater than that on the advancing side (A.S.). Furthermore, it can be seen that the flash formed on the R.S. is larger than that on the A.S. This result corresponds to the experimentally observed behavior of flash formation [38], indicating that the numerical analysis successfully reproduces the actual phenomenon. It should be noted that the tool geometry shown in Fig. 10 differs from that in Fig. 3 because plastic deformation of the tool occurs during the plunging process, and the deformed configuration at the corresponding time step is visualized here.

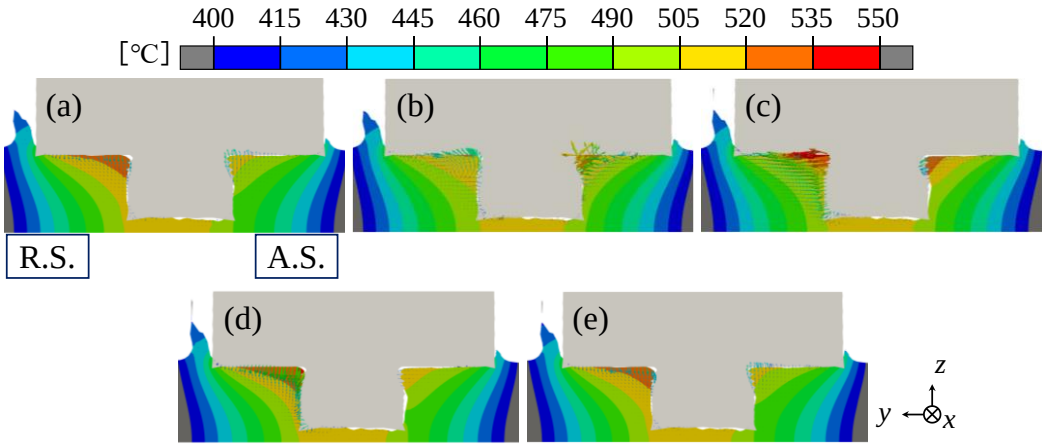

Fig. 10 Temperature and flow velocity distribution during one rotation of bonding at tool center cross section. (a) Start of rotation. (b) 1/4 rotation. (c) 1/2 rotation. (d) 3/4 rotation. (e) 1 rotation

Fig. 11 shows the flow behavior of nine tracer points placed near the tool at 4.8 seconds after the start of welding. Fig. 11(a) presents the initial state, where the tracers are arranged 3.0 mm in the welding direction from the tool center, at a depth of 0.8 mm from the plate surface, and spaced at 2.0 mm intervals in the width direction. Figs. 11(b)-(e) illustrate the movement trajectories of each tracer over the subsequent 2.5 seconds. The tracer motion was calculated based on the material flow velocity at each time step and the time increment. The figure reveals that the tracers flow along the tool rotation direction and that the flow velocity on the retreating side (R.S.) is greater than that on the advancing side (A.S.). It is also evident that the tracer velocities are lower than the tool's rotational speed and decrease with distance from the probe. Furthermore, some tracers are observed to circulate multiple times around the probe. These results are in good agreement with experimentally observed flow behavior [39,40], indicating that the proposed numerical simulation method can successfully reproduce the actual phenomena.

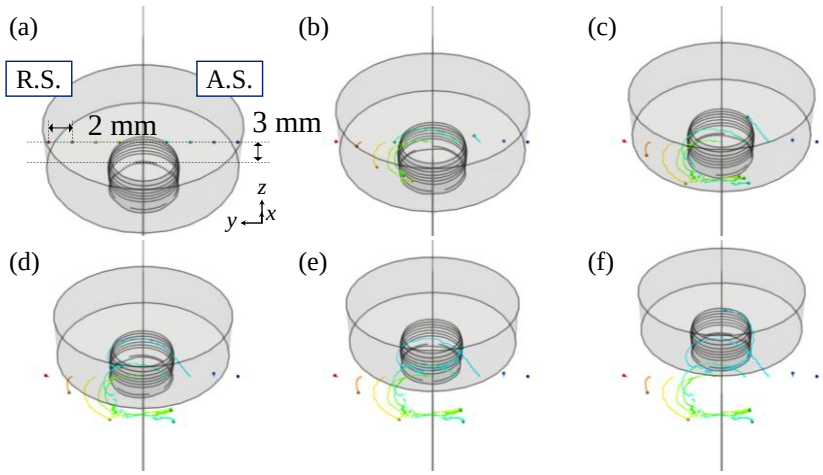

Fig. 11 Flow behavior near tool during welding. (a) Start of rotation. (b) After 0.5 seconds. (c) After 1.0 seconds. (d) After 1.5 seconds. (e) After 2.0 seconds. (f) After 2.5 seconds

Based on these results, the present analysis method is shown to accurately reproduce real phenomena and demonstrates its effectiveness for analyzing the behavior of the workpiece material.

INVESTIGATION OF THERMAL AND FLOW BEHAVIOR OF THE WORKPIECE

Fig. 12 shows the temperature distribution on the tool surface at each stage of the process. Figs. 12(a)-(d) correspond to the tool insertion stage, while Figs. 12(e)-(g) depict the results after the completion of insertion. It can be observed that during insertion, the highest temperature occurs at the tip edge of the probe. After insertion is completed, the surface temperature of the tool decreases and remains mostly below 480 °C. These results suggest that under the present conditions, the strength at the probe tip edge significantly decreases during insertion, indicating a high possibility of wear or damage.

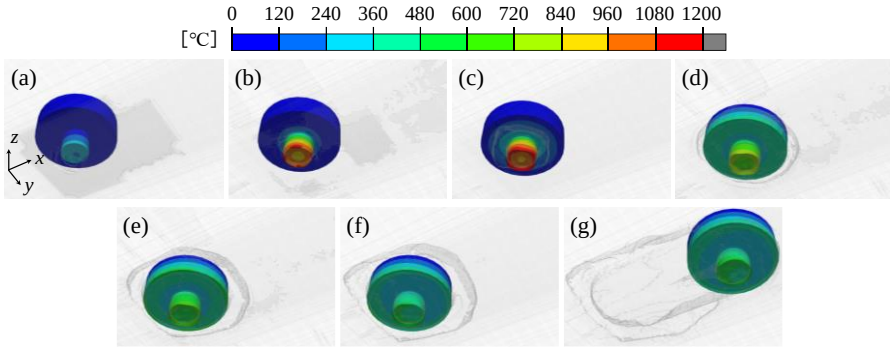

Fig. 12 Temperature distribution on tool surface at each stage. (a) Pin insertion: 0 mm. (b) Pin insertion: 1 mm. (c) Pin insertion: 2 mm. (d) Pin insertion: 3 mm. (e) Plunging completed. (f) Dwelling completed. (g) During welding

Similarly, Fig. 13 presents the equivalent stress distribution on the tool surface during each stage. The results show that in all stages, a high stress concentration occurs at the boundary between the probe and shoulder. This is particularly evident during the welding stage involving tool movement, where even higher stresses are generated. These findings indicate that under the present conditions, relatively high stress is generated at the probe-shoulder boundary during welding, which may potentially increase the mechanical load on the tool.

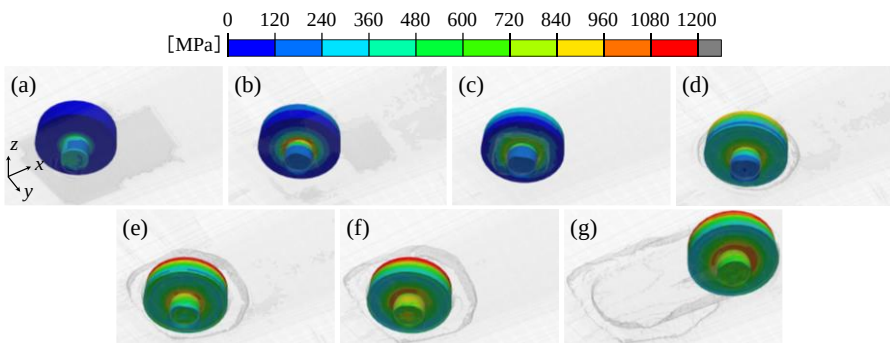

Fig. 13 Equivalent stress distribution on tool surface at each stage. (a) Pin insertion: 0 mm. (b) Pin insertion: 1 mm. (c) Pin insertion: 2 mm. (d) Pin insertion: 3 mm. (e) Plunging completed. (f) Dwelling completed. (g) During welding

Fig. 14 shows the load history acting on the tool. Fig. 14(a) illustrates the load variation from insertion to retraction, and Fig. 14(b) presents the detailed load behavior over 0.6 seconds during welding. From Fig. 14(a), it is confirmed that the vertical load reaches its maximum during the insertion stage. This trend is consistent with prior studies and experimental observations [41], though dependent on the process conditions. Moreover, the loads in the welding and width directions reach their peaks during the welding stage. Furthermore, after

plunging is completed, significant periodic fluctuations are observed in the load components along the welding and width directions. Fig. 14(b) shows that these oscillations have a period corresponding to one tool rotation, suggesting that the periodicity in the load originates from tool rotation. This result is consistent with experimental observations reporting periodic load fluctuations synchronized with tool rotation [8], and also correlates well with the previously discussed temperature distribution periodicity.

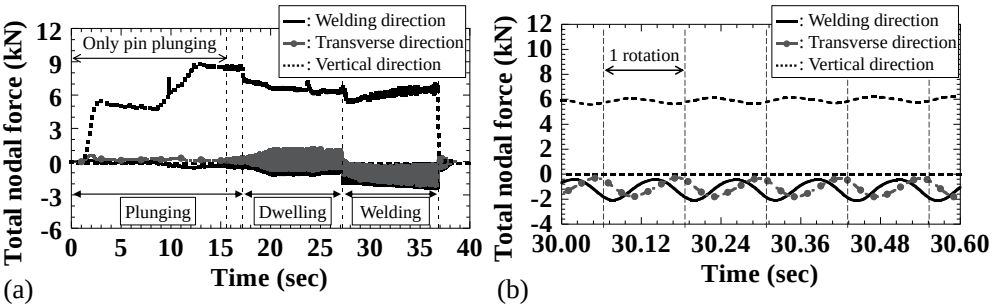

Fig. 14 Tool load history. (a) Entire process. (b) Details during joining

Based on these results, the proposed numerical analysis method is shown to effectively capture key features of the actual phenomena, suggesting its potential usefulness for analyzing tool behavior.

In this analysis, 5,772 nodes were used for the tool and 1,219,581 nodes for the workpiece to simulate the entire FSP process over 38.52 seconds. The total computation time was approximately 212 hours, yielding a computational efficiency of about 5.5 hours per second of physical time. Compared to previous FSW studies employing explicit dynamic CEL analysis [9,10], this represents a large-scale and highly efficient simulation in terms of both element count and analysis time. Furthermore, the use of an implicit formulation enabled the use of larger time steps while maintaining numerical stability and solution accuracy. These characteristics demonstrate the effectiveness and robustness of the proposed analysis method.

EFFECT OF TOOL TILT ANGLE ON THERMAL STATE AND DEFECT FORMATION DURING FSP

In this chapter, a series of simulations were conducted by varying the tool tilt angle based on the welding conditions presented in the previous chapter, with the aim of examining its influence on the temperature field and defect formation. Additionally, this analysis aimed to demonstrate that the proposed simulation method is applicable to defect prediction and can contribute to elucidating the mechanisms of defect formation. As shown in Fig. 15, tool tilt angles of 3° (as used in the previous chapter), 0°, and -3° (forward tilt) were investigated. In this figure, the front and rear sides are defined with respect to the welding direction. In this study, the front and rear sides are defined with respect to the welding direction, where the

front side corresponds to the advancing direction of the tool and the rear side (behind) corresponds to the trailing direction.

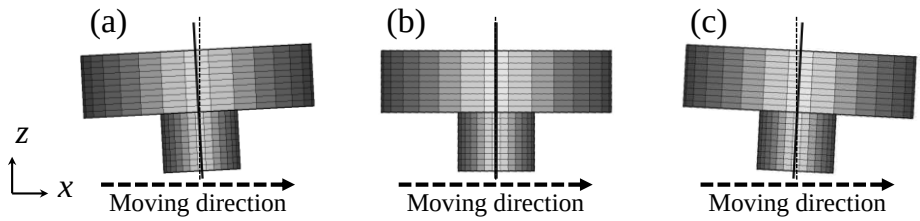

Fig. 15 Tool tilt angle configurations used in analysis. (a) Tilt angle: 3 °. (b) Tilt angle: 0 °. (c) Tilt angle: -3 °

Fig. 16 presents the temperature distributions on the surface of the workpiece near the tool at 4.8 seconds after the start of welding. When the tool tilt angle is 3°, a high-temperature region is observed behind the tool, consistent with the results shown previously. In contrast, when the tilt angle is changed to 0° and -3°, the high-temperature region shifts toward the front side of the tool. Moreover, under the 0° and -3° tilt conditions, surface defects are observed, with the -3° condition showing particularly elongated defects along the welding direction.

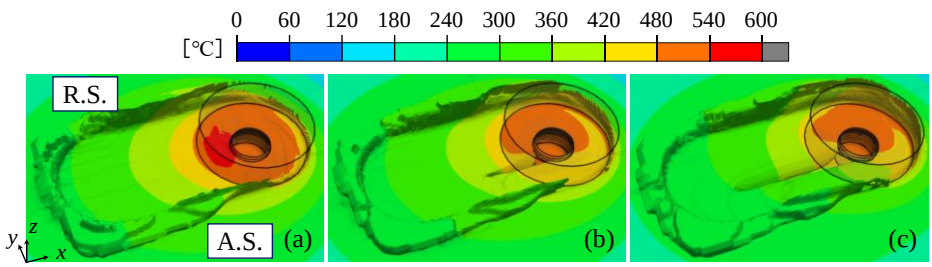

Fig. 16 Temperature distribution on plate surface during welding at each tool angle. (a) Tilt angle: 3 °. (b) Tilt angle: 0 °. (c) Tilt angle: -3 °.

Fig. 17 illustrates the distribution of defects for each tool tilt condition. The defects shown in the figure are located within 1.0 mm from the surface, and the color represents the position in the thickness direction measured from the bottom surface of the plate. As shown in Fig. 17(a), under the 3° tilt condition, only a small void is observed near the advancing side (A.S.) at the probe tip inside the plate. On the other hand, when the tool tilt angle is changed forward to 0° and -3°, the defect region expands, and tunnel-like defects reaching the surface are clearly visible, as described earlier. This relationship between tool tilt angle and defect formation is consistent with experimental observations [42,43], suggesting that the numerical analysis effectively reproduces the actual physical phenomena.

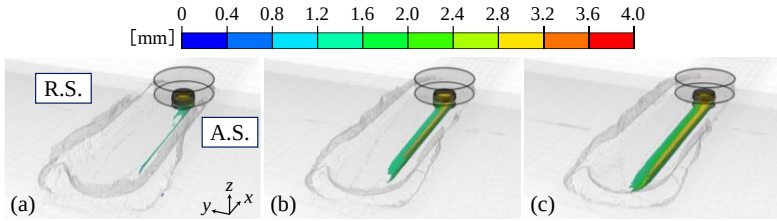

Fig. 17 Distribution of defects during welding at each tool angle. (a) Tilt angle: 3 °. (b) Tilt angle: 0 °. (c) Tilt angle: -3 °

Fig. 18 shows the material flow behavior under different tool tilt angle conditions over a 0.6-second period starting 4.8 seconds after the beginning of welding. Fig. 18(a) presents the initial positions of the tracers placed around the tool. Excluding the probe region, the tracers were arranged at 2.0 mm intervals in both the welding and width directions, and from 0.4 mm to 1.0 mm in the thickness direction from the top surface of the plate. Figs. 18(b) to (d) show the results for each tool tilt angle condition.

From these figures, it can be observed that with a tilt angle of 3.0°, significant material flow occurs behind the tool. In contrast, as the tilt angle becomes more forward-leaning (0° and -3°), the flow behind the tool decreases while the flow in front increases. This trend corresponds to the distribution of high-temperature regions shown in Fig. 16, suggesting that the forward-leaning tool shifts the high-temperature region forward, suppressing rear-side material flow and contributing to defect enlargement.

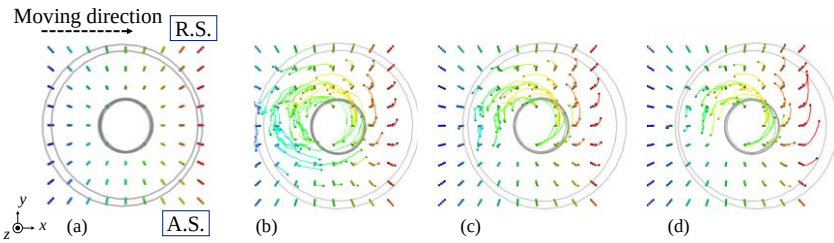

Fig. 18 Effect of tool tilt angle on material flow behavior near tool. (a) Initial position. (b) Tilt angle: 3 °. (c) Tilt angle: 0 °. (d) Tilt angle: -3 °

These results indicate that adjusting the tool tilt angle enables control over the region where intense stirring occurs, thereby revealing part of the mechanism by which tilt angle influences defect formation.

CONCLUSION

In this study, a thermal elastic-plastic analysis method was developed by combining a Coupled Eulerian-Lagrangian (CEL) approach based on an implicit formulation with an idealized

explicit FEM solver optimized for GPU parallel computation. This method was applied to FSP (Friction Stir Processing) analysis of aluminum alloy AA5083, yielding the following findings:

1. Temperature distributions and load fluctuations corresponding to one rotation of the tool were confirmed, successfully reproducing behaviors consistent with experimentally observed periodic formation of onion rings and periodic tool loads.
2. Changes in the tool tilt angle significantly altered the location of high-temperature regions and concentrated material flow. In particular, a forward tilt caused tunnel defects to form and expand toward the surface.
3. The occurrence and extent of defects were found to be closely related to the thermal conditions and material flow history around the tool. The influence of tilt angle on the defect formation mechanism was quantitatively clarified.
4. The analysis was successfully performed with over 1.2 million nodes assigned to the tool and base material, achieving a computational efficiency of approximately 5.5 hours per second of physical phenomena. The results demonstrate that the method maintains both numerical stability due to the implicit formulation and a high degree of physical fidelity and computational feasibility.

References

[1] R. W. FONDA and J. F. BINGERT: 'Texture variations in an aluminum friction stir weld', *Scripta Materialia 57*, pp. 1052-1055, 2007.

[2] M. DHONDT, I. AUBERT, N. SAINTIER and J.-M. OLIVE: 'Mechanical behavior of periodical microstructure induced by friction stir welding on Al–Cu–Li 2050 alloy', *Materials Science and Engineering A 642*, pp. 163-172, 2015.

[3] W. F. NOH: 'CEL: A Time-Dependent, Two-Space-Dimensional, Coupled Eulerian-Lagrangian Code', *Lawrence Radiation Laboratory, University of California*, pp. 1-48, 1964.

[4] M. AKBARI, P. ASADI and T. SADOWSKI: 'A Review on Friction Stir Welding/Processing: Numerical Modeling', *Materials 16*, 5890, 2023.

[5] M. AKBARI, A. ABDOLLAHZADEH and M. ESFANDIAR: 'A Comprehensive Review of Material Flow in FSW/FSP: Experimental Insights and Simulation Perspectives', *Engineering Reports 7*, e70138, 2025.

[6] DASSAULT SYSTÈMES: 'Modeling Extreme Deformation and Fluid Flow with Abaqus', *SIMULIA Training Course Documentation*, 2017.

[7] D. DAS, S. BAG and S. PAL: 'Probing finite element modelling of defects in friction stir welding by tailoring mass scaling factor', *Materials Today Communications 35*, 105646, 2023.

[8] D. AMBROSIO, A. TONGNE, V. WAGNER, G. DESSEIN and O. CAHUC: 'Towards material flow prediction in friction stir welding accounting for mechanisms governing chip formation in orthogonal cutting', *Journal of Manufacturing Processes 85*, pp. 450-465, 2023.

[9] M. HOSSFELD and E. ROOS: 'A new approach to modelling friction stir welding using the CEL method', *International Conference on Advanced Manufacturing Engineering and Technologies*, pp. 1-9, 2013.

[10] M. HOSSFELD: 'Modeling Friction Stir Welding: On Prediction and Numerical Tool Development', *Metals 12*, 1432, 2022.

[11] P. CHAUHAN, R. JAIN, S. K. PAL and S. B. SINGH: 'Modeling of defects in friction stir welding using coupled Eulerian and Lagrangian method', *Journal of Manufacturing Processes 34*, pp. 158-166, 2018.
[12] K. N. SALLOOMI: 'Fully coupled thermomechanical simulation of friction stir welding of aluminum 6061-T6 alloy T-joint', *Journal of Manufacturing Processes 45*, pp. 746-754, 2019.
[13] K.N. SALLOOMI and S. AL-SUMAIDAE: 'Coupled Eulerian–Lagrangian prediction of thermal and residual stress environments in dissimilar friction stir welding of aluminum alloys', *Journal of Advanced Joining Processes 3*, 100052, 2021.
[14] D. J. BENSON: 'Computational Methods in Lagrangian and Eulerian Hydrocodes', *Computer Methods in Applied Mechanics and Engineering 99*, pp. 235-394, 1992.
[15] N. M. NEWMARK: 'A Method of Computation for Structural Dynamics, Journal of the Engineering Mechanics Division', *Proceedings of the American Society of Civil Engineers 85-EM-3*, pp. 67-94, 1959.
[16] M. SHIBAHARA and K. IKUSHIMA: 'Development of analytical method for welding mechanics using idealized explicit FEM', *Transactions of JWRI 39-2*, pp. 384-386, 2010.
[17] M. SHIBAHARA, K. IKUSHIMA, S. ITOH AND K. MASAOKA: 'Computational Method for Transient Welding Deformation and Stress for Large Scale Structure Based on Dynamic Explicit FEM', *Quarterly Journal of the Japan Welding Society 29-1*, pp. 1-9, 2011.
[18] K. IKUSHIMA, M. SHIBAHARA, K. AKITA, H. SUZUKI, S. MOROOKA, S. NISHIKAWA and T. FURUKAWA: 'Numerical analysis of residual stress distribution on peening process', *Weld World 61*, pp. 517-527, 2017.
[19] A.N. BROOKS and T.J.R. HUGHES: 'Streamline Upwind/Petrov-Galerkin Formulations for Convection Dominated Flows with Particular Emphasis on the Incompressible Navier-Stokes Equations', *Computer Methods in Applied Mechanics and Engineering 32*, pp. 199-259, 1982.
[20] T.J.R. HUGHES, G. SCOVAZZI and T.E. TEZDUYAR: 'Stabilized Methods for Compressible Flows', *Journal of Scientific Computing 43*, pp. 343-368, 2010.
[21] E. L. WILSON and R. W. CLOUGH: 'Dynamic Response by Step-By-Step Matrix Analysis', *Proceedings of the Symposium on the Use of Computers in Civil Engineering*, Lisbon, Portugal, 1962.
[22] S. MOHAMMADZADEH, M. GHASSEMIEH and Y. PARK: 'Structure-dependent improved Wilson-θ method with higher order of accuracy and controllable amplitude decay', *Applied Mathematical Modelling 52*, pp. 417-436, 2017.
[23] S.-L. ZHANG: 'GPBi CG: Generalized Product Type Methods Based on Bi CG for Solving Nonsymmetric Linear Systems', *SIAM Journal on Scientific Computing 18-2*, pp. 537-551, 1997.
[24] X.-F. ZHANG, W. DING and T. LI: 'Tensor form of GPBiCG algorithm for solving the generalized Sylvester quaternion tensor equations', *Journal of the Franklin Institute 360*, pp. 5929-5946, 2023.
[25] K. IKUSHIMA and M. SHIBAHARA: 'Prediction of residual stresses in multi-pass welded joint using Idealized Explicit FEM accelerated by a GPU', *Computational Materials Science 93*, pp. 62-67, 2014.
[26] K. IKUSHIMA, S. ITOH and M. SHIBAHARA: 'Development of Idealized Explicit FEM Using GPU Parallelization and Its Application to Large-Scale Analysis of Residual Stress of Multi-Pass Welded Pipe Joint', *Weld World 59*, pp. 589-595, 2015.
[27] C. W. HIRT and B. D. NICHOLS: 'Volume of Fluid (VOF) Method for the Dynamics of Free Boundaries', *Journal of Computational Physics 39*, pp. 201-225, 1981.

[28] O. C. ZIENKIEWICZ, W. L. WOOD, N. W. HINE and R. L. TAYLOR: 'A unified set of single step algorithms. Part 1: General formulation and application', *International Journal for Numerical Methods in Engineering 20-15*, pp. 1529-1552, 1978.

[29] J.J. MASON, A.J. ROSAKIS and G. RAVICHANDRAN: 'On the Strain and Strain Rate Dependence of the Fraction of Plastic Work Converted to Heat: An Experimental Study Using High Speed Infrared Detectors', *Mechanics of Materials 17*, pp. 135-145, 1994.

[30] J. HODOWANY, G. RAVICHANDRAN, A. J. ROSAKIS and P. ROSAKIS: 'Partition of Plastic Work into Heat and Stored Energy in Metals', *Experimental Mechanics 40*, pp. 113-123, 2000.

[31] G. R. JOHNSON and W. H. COOK: 'A Constitutive Model and Data for Metals Subjected to Large Strains, High Strain Rates and High Temperatures', *Proceedings of the 7th International Symposium on Ballistics*, pp. 541-547, 1983.

[32] R. V. MISES: 'Mechanics of solid bodies in the plastically-deformable state', *Nachr. d. Kgl. Ges. Wiss. Göttingen, Math.-phys. Klasse 4*, pp. 582-592, 1913.

[33] M. YU, N. MA, K. NARASAKI, S. TSUTSUMI and H. FUJII: 'Modelling and Measurement of Thick Aluminum FSW Induced Thermal Strain and Residual Stress', *Journal of Light Metal Welding 59-2*, pp. 59-68, 2021.

[34] H. SHI, J.-R. CHO, J.-W. YOON, H.-J. LEE and D.-G. AHN: 'Design of Thermal Stress Control Layers in the Selective Deposition Technology of Hot Axle Forging Dies', *International Journal of Precision Engineering and Manufacturing 18-12*, pp. 1805-1812, 2017.

[35] D.-S. GUK, H.-J. LEE and D.-G. AHN: 'A study on the Effects of Geometrical Parameters of Overlay Coated Layer on the Thermal Stress-strain Distributions of Co-based Super-alloy Deposited Layer on Hot-working Tool Steel', *MATEC Web of Conferences 40*, 01003, 2016.

[36] NIPPON KOSHUHA STEEL CO., LTD.: *KDA1 Series of Thermocouples for Welding*, https://www.koshuha.co.jp/eng/products/kda1.html, accessed 2025-07-28.

[37] M. DHONDT, I. AUBERT, N. SAINTIER and J.M. OLIVE: 'Characterization of intergranular stress corrosion cracking behavior of a FSW Al-Cu-Li 2050 nugget', *Mechanics & Industry 16*, 401, 2015.

[38] T. MARAZANI, S. O. JEJE, M. B. SHONGWE and N. MALATJI: 'Mass flash reduction strategies in friction stir processing of aluminum alloys: A review', *Engineering Reports 6-10*, e12981, 2024.

[39] Y. MORISADA, H. FUJII, Y. KAWAHITO, K. NAKATA and M. TANAKA: 'Three-dimensional visualization of material flow during friction stir welding by two pairs of X-ray transmission systems', *Scripta Materialia 65*, pp. 1085-1088, 2011.

[40] R. KUMAR, V. PANCHOLI and R.P. BHARTI: 'Material flow visualization and determination of strain rate during friction stir welding', *Journal of Materials Processing Technology 255*, pp. 470-476, 2018.

[41] V. SOUNDARARAJAN, S. ZEKOVIC and R. KOVACEVIC: 'Thermo-mechanical model with adaptive boundary conditions for friction stir welding of Al 6061', *International Journal of Machine Tools and Manufacture 45*, pp. 1577-1587, 2005.

[42] L. LONG, G. CHEN, S. ZHANG, T. LIU and Q. SHI: 'Finite-element analysis of the tool tilt angle effect on the formation of friction stir welds', *Journal of Manufacturing Processes 30*, pp. 562-569, 2017.

[43] S. D. MESHRAM and G. M. REDDY: 'Influence of Tool Tilt Angle on Material Flow and Defect Generation in Friction Stir Welding of AA2219', *Defence Science Journal 68*, pp. 512-518, 2018.